Inhalation Toxicology

http://informahealthcare.com/iht
ISSN: 0895-8378 (print), 1091-7691 (electronic)

Inhal Toxicol, 2013; 25(5): 280–291
 DOI: 10.3109/08958378.2013.781250

informa
healthcare

RESEARCH ARTICLE

Source and trajectories of inhaled particles from a surrounding environment and its deposition in the respiratory airway

Kiao Inthavong[1,2], Qin Jiang Ge[1], Xiangdong Li[1], and Ji Yuan Tu[1,2,3]

[1]School of Aerospace, Mechanical and Manufacturing Engineering and [2]Platform Technologies Research Institute, RMIT University, Bundoora, VIC, Australia, and [3]Department of Building Science, Tsinghua University, Beijing, China

Abstract

The inhalation exposure to airborne particles is investigated using a newly developed computational model that integrates the human respiratory airway with a human mannequin and at an enclosed room environment. Three free-stream air flow velocities (0.05, 0.20, and 0.35 m s^{-1}) that are in the range of occupational environments are used. Particles are released from different upstream locations and their trajectories are shown, which revealed that the trajectory paths of 80 μm particles that are inhaled are the same from the three different upstream planes evaluated. Smaller particles, 1 and 10 μm, exhibited different inhalation paths when released from different upstream distances. The free-stream velocity also has an effect on the particle trajectory particularly for larger particles. The aspiration efficiency for an extended range of particle sizes was evaluated. Reverse particle tracking matches the deposition in the respiratory airway with its initial particle source location. This can allow better risk assessments, and dosimetry determination due to inhalation exposure to contaminant sources.

Keywords

Aspiration efficiency, computational fluid dynamics, deposition, indoor air, inhalation, nasal cavity

History

Received 16 October 2012
Revised 15 February 2013
Accepted 26 February 2013
Published online 24 April 2013

Introduction

Exposure to harmful contaminants in indoor environments has substantial bearing on an occupants' health. Incidences of bioterrorism and industrial mishaps have demonstrated a need to understand the transmission and exposure risks. Examples include the contaminant exposure from a local source such as a contaminated letter containing anthrax (Agranovski et al., 2005; Scott Duncan et al., 2009); formaldehyde and asbestos from building materials (Ganor et al., 1992; Repace, 1982); and microbial infectious contaminants in offices, hospitals, shopping centres and large indoor spaces (Bolashikov et al., 2012; Kelland, 1992).

The adverse health responses are apt to the exposure of indoor airborne contaminants. A number of publications have demonstrated the extensive studies undertaken to investigate the dispersion of contaminants in indoor environments released from a source (Namieśnik et al., 1992; Nazaroff, 2004). The contaminant source wields major influence on the dispersion and therefore exerts exposure risk to an occupant. While the cited studies have shown how the contaminants are dispersed, their eventual deposition in the respiratory tract was not included. Identification of inhaled contaminants from an upstream location may facilitate the assessment of the risk to occupants and determine methods of evaluation to reduce the exposure during unintentional release of airborne toxic contaminants.

Experimental measurements of particle inhalability have been performed by Kennedy & Hinds (2002), they used a full-size, full-torso mannequin to collect dust entering either the mouth or nose during breathing. Later Li et al. (2007), Anthony et al. (2005), and King Se et al. (2010) used computational fluid dynamics (CFD) modeling to study the inhalability of airborne particles and found that the complex features of the human face-affected particle aspiration in low-velocity environments. They concluded that particle diameter and breathing velocity and to a lesser extent facial feature dimensions were the main influencing factors on determining exposure estimates in low free-stream velocities. In these studies, the trajectory of inhaled particles travelling through the flow field from a given location is shown. However, the distance between the nose and the upstream particle source location was not consistent among the studies. In this study, it is hypothesized that different location sources may affect the trajectories of inhaled particles, and that this may have an effect on the particle inhalability, referred to as the aspiration efficiency (AE), and further on the deposition rates in the respiratory airway.

Therefore, as a step toward establishing a computational platform for predicting the upstream contaminant source in indoor air exposure, this study presents a new modeling strategy by integrating the inner respiratory airflow with a human body and the indoor air and particle. This differs from traditional modeling that separates the inner respiratory airway from the outer airflows. The influences of airflow

Address for correspondence: Prof. Jiyuan Tu, School of Aerospace, Mechanical and Manufacturing Engineering, RMIT University, PO Box 71, Bundoora, VIC 3083, Australia. Tel: +61-3-9925-6191. Fax: +61-3-9925-6108. E-mail: jiyuan.tu@rmit.edu.au

Table 1. Body and facial details.

Human occupant details			Facial details		
Dimension	Present study	50th % man[a]	Dimension	Present study	50th % man[b]
Occupant height	170.0	175.9	Head length	18.3	19.5
Mid shoulder height	139.7	144.4	Head circumference	56.3	56.8
Head width	13.5	15.5	Face length	9.1	11.8
Head depth	18.3	19.6	Face width	13.5	14.1
Top of head to chin	19.2	22.1	Nose length	4.13	5.0
Top of head to mouth centre	15.2	18.0	Nose protrusion	1.56	2.1
Top of head to eyes	9.2	11.5	Nose breadth	3.79	3.4

All units are in centimetres [cm].
[a]Huston (2009).
[b]Zhuang et al. (2010).

patterns on the transport of indoor particle contaminants are evaluated. Particle trajectories released from different upstream locations are visualized using a Lagrangian particle-tracking technique, the origins of the upstream particles that are inhaled can be determined and compared with the simplified analytical solutions. This can greatly assist in determining contaminant sources that are likely to be inhaled and preventative measures such as placement of local ventilation can be put into place.

Methods

Computational geometry

Several CFD models of individual regions of the human respiratory airway have been created (based on computed tomography (CT) scans of Asian male volunteers) by Inthavong et al. (2009, 2011c). The conversion from CT scans to a three-dimensional (3D) model is primarily based on a semi-automated image-processing technique (segmentation), which extracts a contiguous airway path from the nostril inlets to the upper trachea. In addition to the nostrils, a partial region of the external nose, proximal to the nostrils was included. A 3D head was created that contained detailed facial features, made to specific dimensions (Table 1) that was representative of the 50th percentile of an American male, as described in the literature (Huston, 2009; Zhuang et al., 2010).

A simple mannequin body shape was created and placed in an external empty room to allow ambient air flow. A limitation of this simplified body shape is that the legs are not separated, but rather placed together. In situations where the legs are apart, it has been shown that some differences can be found (Ge et al., 2013). The integrated model is shown in Figure 1. The coordinate system is created so that the origin point (0,0,0) is taken at the midline point of the face and at the nostril tip height. Additional details in the figure include upstream particle release plane, detailed facial features and the internal nasal-to-trachea respiratory airway cavity that is adjoined to the nostrils.

The meshing requirements for the CFD model present a challenge because the geometric dimensions span multiple length scales from meter lengths of the room down to centimeters within the trachea. This step involved meshing the model sequentially from the internal respiratory airway and then outward into the external room. Prism layers were applied to the bounding respiratory walls, and a tetrahedral unstructured mesh filled the airway passage. The final model of the respiratory airway alone consisted of 11 million cells. Preliminary flow modeling testing showed that the model was highly susceptible to numerical artificial diffusion, i.e. false diffusion, primarily caused by the unidirectional convective flow and difference in size between the largest and smallest unstructured mesh element. To minimize false diffusion, incremental mesh refinement was performed in order to obtain a gradual expansion from the smallest elements within the respiratory airway to the larger mesh elements in the outer room. Simulations were performed after each increment, and a quick qualitative velocity contour comparison in a cross-section of the airway with literature data was made.

To ensure the quality of results, and a high level of mesh integrity, a mesh independence test was performed by investigating the velocity profiles at a number of different locations (e.g. inside the nasal cavity, near the breathing zone) until the profiles converged. The mesh became convergent at 8 million cells. However, to minimize any false diffusion caused by the unstructured mesh, a conservative final computational model of 16 million cells was used, which required 912 Mb in storage space per simulated case. A similar work to use such a high-resolution mesh is that of Doorly et al. (2008). Earlier studies by the authors found that a mesh in excess of 2.0 million cells provided grid independence for the nasal cavity region (Inthavong et al., 2011a) among other studies (Golshahi et al., 2010; Lee et al., 2010; Moghadas et al., 2011), while a mesh of 1.2 million cells was sufficient for grid independence of the room with human occupant model (King Se et al., 2010). The visualization and generation of the mesh was possible on a PC computer with 32 Gb Ram, and 8 processor cores. The simulations were performed on a High-Performance Computing cluster of 268 processor cores.

Airflow modeling

Kennedy & Hinds (2002) showed that ''facing-the-wind'' orientation produces an upper limit for inhalability compared with an averaged orientation produced by equally weighting inhalability over all angles from 0 to 360°. Selection of the airflow speed was based on the Baldwin & Maynard (1998) review of airflow speeds in various occupational workplaces, which found a mean value of 0.3 m s^{-1} (ranging from 0.04 to

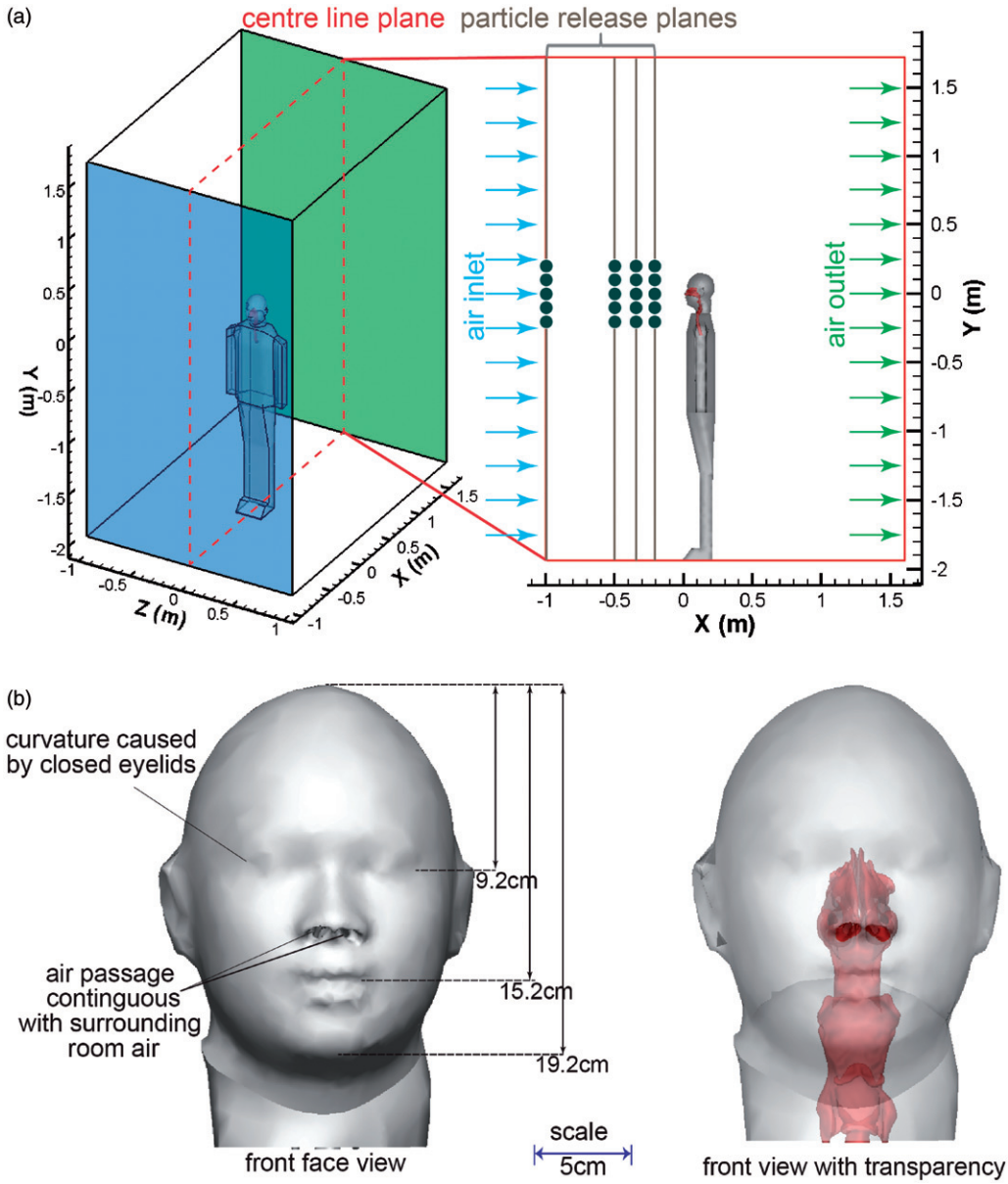

Figure 1. (a) 3D CAD model incorporating the external surrounding room, human occupant, and the internal nasal-pharynx-larynx-trachea respiratory airway model. (b) Front view showing the detailed facial features. Geometry dimensions and details of the room and human occupant are given in Tables 1 and 2. The coordinate (0,0,0) is taken at the midline point of the face, at the nostril tip height.

2.02 m s^{-1}). After neglecting one set of skewed data, a mean of 0.2 m s^{-1} (ranging from 0.04 to 0.72 m s^{-1}) was found. In an office environment, the airflow speeds ranged from 0.011 to 0.164 m s^{-1}. In this study, three different indoor airflow velocities (0.05, 0.20, and 0.35 m s^{-1}) were investigated. For dynamic similarity, matching the Reynolds number over the head of the mannequin for the CFD model was made in comparison with existing experimental data by Anthony et al. (2005). This required the free-stream velocity to be set at 0.2 m s^{-1}, and for oral inhalation, the Reynolds number is 1590, which requires an inhalation velocity of 1.78 m s^{-1}, equivalent to 24 liters per minute (LPM). The inhalation flow is produced by setting the boundary at the trachea outlet to a negative pressure to achieve the desired flow rate. Further details of the inhalation and room flow details are given in Table 2.

For indoor airflows, the k-ε-RNG model has been shown to provide better flow separation and reattachment

Table 2. Inhalation and room flow details.

Dynamic similarity		
	Present study	Anthony et al. (2005)
$Re_{free\ stream}$ (room inlet)	48 000	50 250
Re_{head}	1955	1909
Head width	14.8 cm	9.6 cm
$U_{free\ stream}$	0.2 m s^{-1}	0.3 m s^{-1}
Anthony et al. (2005) data is for 101 pm case only		
Re_{inhale}	1590	1590
Characteristic length	1.35 cm	0.887 cm
Mouth area	2.25 cm^2	0.618 cm^2
Inhalation velocity	1.78 m s^{-1}	2.7 m s^{-1}
	Right	Left
Nostril area	1.52 cm^2	1.31 cm^2
Perimeter	4.72 cm	4.62 cm
D_h	1.29 cm	1.13 cm

*Characteristic length is defined here as the hydraulic diameter, $D_h = 4A/P$, where A = area, P = perimeter.

(Hofmann et al., 2003), which is an expected flow feature of passing over the head. However, in the human respiratory system, many researchers have used k–ω turbulent model with Shear Stress Transport (SST) developed by Menter et al. (2006) to analyze airflow in the nasal cavity (Longest et al., 2012; Zhu et al., 2011). For nasal inhalation, a constant flow rate of 15 LPM is used which is the same flow rate that has been used in earlier studies by Inthavong et al. (2009, 2011c) to allow direct comparisons of the particle deposition results. The SST-transition model has been applied to the internal respiratory flows; however, its performance on the indoor airflow is unknown. This raises the issue of selecting a suitable turbulence model that will accommodate both the flow patterns in the indoor room air and inside the small respiratory airways. Given the promising results of the SST-transition model for respiratory airflows by Zhang & Kleinstreuer (2011), the model is first evaluated for the indoor airflow against experimental data and the RNG k-ε model. The continuity and momentum equations are given as follows:

Continuity equation:

$$\frac{\partial}{\partial x_i}\left(\rho_g u_i^g\right) = 0 \tag{1}$$

Momentum equation:

$$\rho_g u_i^g \frac{\partial u_i^g}{\partial x_j} = -\frac{\partial p_g}{\partial x_i} + \frac{\partial}{\partial x_j}\left[\mu_g \frac{\partial u_i^g}{\partial x_j}\right] \tag{2}$$

where ρ, $\bar{U}$, and p are density, velocity, and pressure of the air, respectively.

The turbulence model equations for the RNG k–ε model and the SST-transitional model are given by Isabey & Chang (1981) and Menter et al. (2006) from which the models are formulated, and these are not reproduced here for brevity. Turbulence quantities at the inlets were defined with 5% intensity and its hydraulic diameter. The additional transport equations for k, ε and ω are discretized using the finite volume CFD code, ANSYS-Fluent 14.0. A second-order scheme is used to approximate the momentum equation while the pressure–velocity coupling is handled through the SIMPLE method.

Particle equations

Particles with aerodynamic diameters of 1, 10, 40 and 80 μm are released from upstream planes at 0.2, 0.5, and 1.0 m from the manikin face. Each individual particle was tracked from its source through the external space and the human respiratory system if they enter through the nostrils or mouth. A Lagrangian approach under one-way coupling was used, and thus the particles are considered a dilute disperse phase. The particle tracking was terminated when a particle either reached a boundary surface, whereby it is assumed to deposit, or escaped through the computational domain via the trachea or the outlet boundary of the room. The force balance equation that governs the particle motion is given as

$$\frac{\mathrm{d}u_p}{\mathrm{d}t} = F_D(u_g - u_p) + \frac{g(\rho_p - \rho_g)}{\rho_p}. \tag{3}$$

The drag force, F_D, is dependent on the drag coefficient defined by

$$C_D = a_1 + \frac{a_2}{\mathrm{Re}_p} + \frac{a_3}{\mathrm{Re}_p^2} \tag{4}$$

where the a_1, a_2 and a_3 are empirical constants for smooth spherical particles over several ranges of droplet Reynolds number (Morsi & Alexander, 1972). Gravitational settling is given by g and the density terms, ρ, disappear when the density of the particle is much greater than the fluid such as the case in this study (e.g., $\rho_p \gg \rho_g$).

The turbulent dispersion of the particle is performed through the Discrete Random Walk or ''eddy interaction model''. This approach assumes that a particle interacts with a succession of random discrete turbulent eddies, where each eddy is defined by a lifetime, length and velocity scale. The k–ε and k–ω family of turbulent models are classified as Reynolds-Averaged-Navier-Stokes-based models that assume isotropic turbulent fluctuations. In the turbulent core region, this isotropic assumption is valid in the absence of high swirls and rapid changes in the strain rate; however, close to the wall, the turbulent flow character is highly anisotropic (Matida et al., 2004). An improved model for the random walk method is to apply a damping function to correct the fluctuations in the near wall up to y^+ of 60 as

$$k_{new} = [1 - \exp(-0.02y^+)]^2 k \quad \text{for } y^+ < 60 \tag{5}$$

where k is the turbulent kinetic energy and y^+ is the normalized wall distance. Full details of the scheme can be found in the study by Inthavong et al. (2011a,b), which implemented the damping function to improve the micron particle deposition in the nasal cavity.

A small number of particles (e.g. 10 000) were initially released from different upstream locations in a plane. The locations of these vertical planes were at 0.2, 0.5, and 1.0 m upstream from the nose tip, which is depicted in Figure 1(a). Inhaled particles were tracked back to their origin, which provided a bounding area (known as the critical area) that encompasses all inhaled particles. Due to the turbulent dispersion, fluctuating velocities in the free stream may cause particles released from outside this initially defined bounding area to be inhaled for any given tracking simulation. As such, subsequent particles were released from a circular area that was approximately twice the size of the initially defined bounding area (Figure 2). The number of particles for tracking was then increased incrementally up to 150 000 which were released from the larger bounding area and uniformly distributed. The number of particles reached statistical independence when the number of particles that entered the airways was 80 000 particles. This was considered the optimum number for statistical independence since an increase of inhaled particles to 120 000 yielded a difference of less than 0.5% in the deposition efficiency.

All particles were released from rest to mimic a contaminant source that is disturbed by the free-stream flow. The relaxation time for 1 μm particles is very short while for 80 μm particles this is much longer. This means that the larger particles (80 and 40 μm) will take a longer time and therefore distance to reach equilibrium with the free-stream velocity

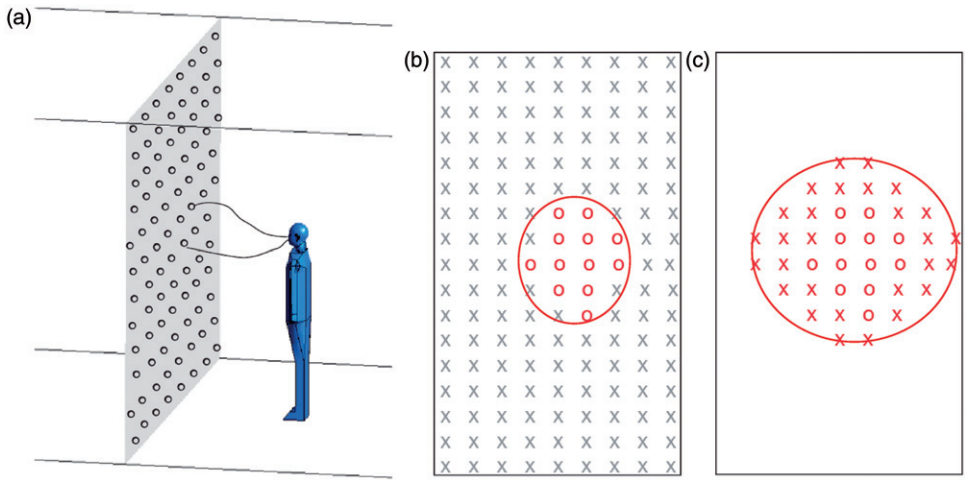

Figure 2. A schematic representation of particle release locations. (a) Particles are initially released uniformly throughout an upstream plane. (b) Inhaled particles are identified on the origin plane, where a bounding area of particles is found. (c) A larger bounding area region for all released particles is used to account for turbulent dispersion. The symbol X represents particles that are not inhaled while the symbol O represents particles that are inhaled.

and gravitational settling. This should be considered if comparisons are made with data produced from airborne particles that are released with free-stream velocities instead of from rest.

Aspiration efficiency

The inhalability of airborne particles from an upstream source was evaluated through the AE, which is a measure of the fraction of particles that are inhaled through the nose or mouth during breathing (Vincent et al., 1990). An empirical correlation for the AE for orientation-averaged mouth inhalation and wind speed of $0.4\,\mathrm{m\,s^{-1}}$ or below has been defined by Vincent et al. (1990) as

$$AE = 0.5(1 + \exp(-0.06 d_{ae})), \quad d_{ae} \leq 100\,\mu\mathrm{m} \qquad (6)$$

where d_{ae} is the aerodynamic diameter. The AE for each particle size was quantified by determining the ratio of the inhaled particle concentration (C) to the ambient free-stream particle concentration (C_∞) where the concentration can be expressed as the number of particles inhaled per volume. King Se et al. (2010) showed that this can be simplified as

$$AE = A_c V_c / A_n V_n \qquad (7)$$

where A_c is the critical area from the upstream source shown in Figure 6, A_n is the nostril inhalation area, and V_c and V_n are the average velocity through the critical and inhalation areas defined.

Results and discussion

Velocity patterns in the breathing region

Velocity profiles taken at a vertical line at $x = 1.5\,\mathrm{cm}$ upstream from the face, along with velocity vectors in the x–y centerline plane (Figure 3) were compared with experimental data for mouth breathing by Anthony et al. (2005) and CFD data for nose breathing by King Se et al. (2010) to verify and provide confidence in the accuracy of the CFD simulations. The profiles obtained from the RNG and SST-transitional turbulence models provide similar results as the oncoming air approaches the face, providing confidence in the modeling. The surrounding environment flow field was quite simple – an open space that is free from any obstructions that could initiate turbulent flow characteristics – and therefore it should not produce significant differences between the two turbulence models tested. Peak velocities were found at the location of inhalation (i.e. mouth or nose region depending on the inhalation route), which was expected. The velocity vectors provide visualization which reveals that in the near breathing region, vectors point vertically upward due to the presence of the torso. Furthermore, the oncoming airflow bifurcates at the nose tip as well as at the chin. Downward flow was found in the philtrum (space between the nose and the upper lip).

For nasal inhalation, airflow was directed upward toward the nostril openings (Figure 3b). The velocity vectors show that the inhaled flow was nearly all directed vertically into the nostrils. This suggests that small particles (i.e. $<2.5\,\mu\mathrm{m}$) will drift with the induced airflow and therefore are likely to be inhaled if found below the inhalation route. In contrast, particles with higher inertia and mass, that are not able to drift with the flow streams, need to be found above the nostrils or mouth to allow for gravitational settling in order for the particles to be inhaled into the respiratory airways. The effect of the vertical flow across the closed mouth region can enhance the inhalability of the particles if breathing through the mouth was also to occur midway through an inhalation cycle. Such a study involving both the nose and mouth inhalation under different breathing situations was not investigated in this study and is left for further studies.

The oncoming stream of air viewed from front in relation to the face is shown in Figure 4. The flow pattern around the face is generally uniform except for around the nostrils where the influence of inhalation is apparent. In this instance, the inhalation flow rate was set to $15\,\mathrm{L\,min^{-1}}$ (representative of resting breathing) which induces an acceleration of fluid within the proximity of the nostrils. Incidentally, this is where the local peak velocities are found. The 2D velocity vectors

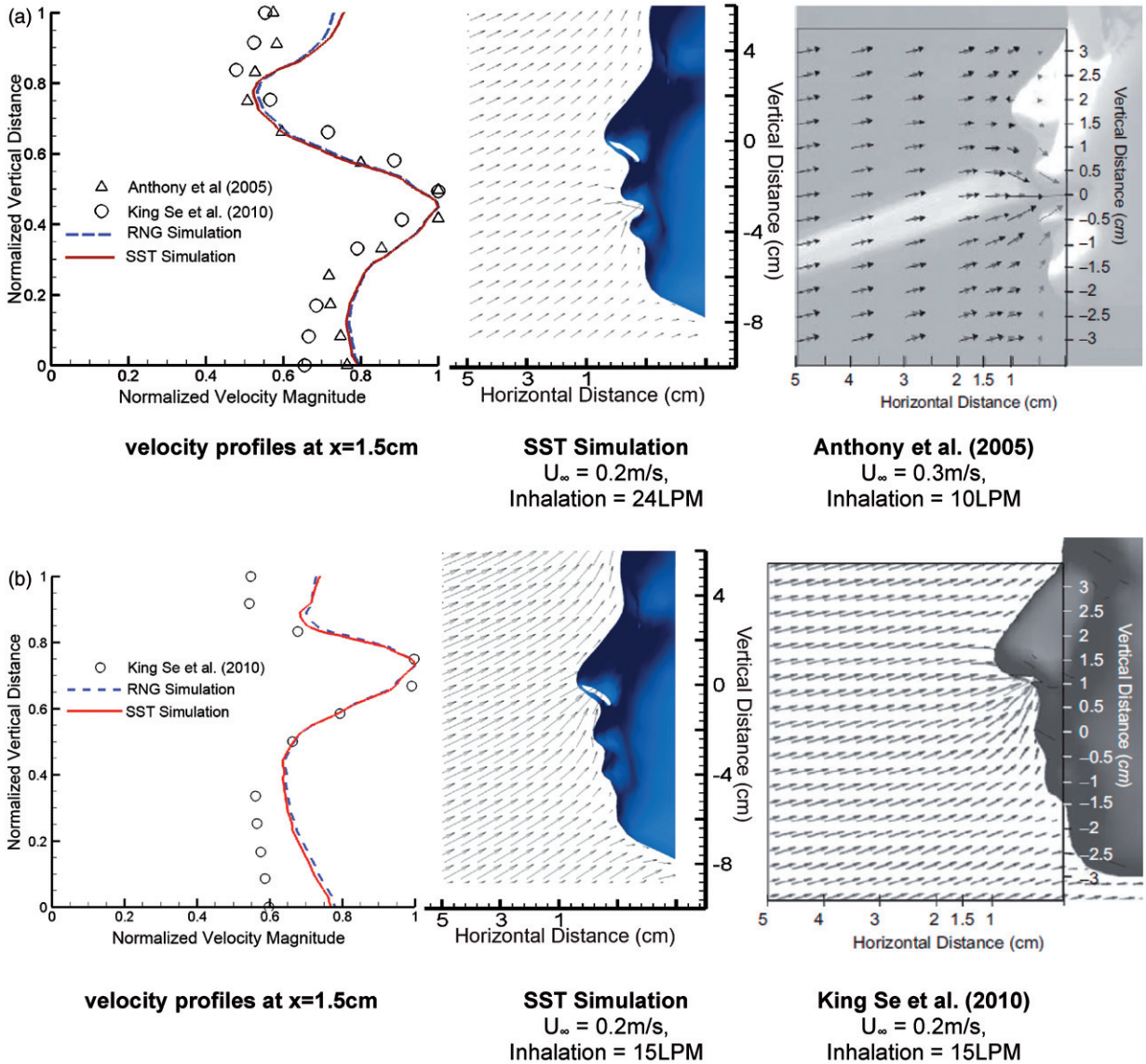

Figure 3. Velocity magnitude profiles taken at 1.5 cm from the nose tip, and velocity vectors in the centerline plane (x–y plane) in comparisons with data in the literature. (a) Oral/mouth breathing. (b) Nasal/nose breathing.

were uniform in length in order to show the direction of the flow in the y–z plane. For a free-stream velocity of 0.05 m s^{-1}, the vertical flow component splits into two directions at the nostril region. Below the nostril openings the flow goes upward, while above the nostril in the region y [−0.004 to 0.025] the flow goes downward. Interestingly, when the flow field was increased to 0.35 m s^{-1} nearly all velocity vectors were directed upward with the region of downward pointing vectors reduced to a small region. This can be seen as a ratio of the influence of the inhalation effort created by nostrils to the oncoming flow velocity. At higher free-stream velocities, the influence of inhalation in the form of accelerated flow toward the nostrils was diminished.

Particle trajectories

The particle motion equation (Equation 3) is in the form of an ordinary differential equation. If it is assumed that the particles exist under Stokes drag, then C_d becomes constant ($C_d = 24/Re$). Furthermore, if the flow field is assumed constant: $\mathbf{u}_f = U_\infty =$ fixed ambient flow velocity, the solution becomes

$$x = x_o + U_\infty t - U_\infty \tau + U_\infty \tau \exp\left(-\frac{t}{\tau}\right);$$

$$y = y_o - V_\infty \tau + \left(g\tau^2 + V_\infty \tau\right)\exp\left(-\frac{t}{\tau}\right) - g\tau^2 + t(V_\infty + g\tau) \quad (8)$$

where U_∞ can be 0.05, 0.20, or 0.35 m s^{-1} for the horizontal free-stream velocity, while V_∞ is zero. The variables x_o and y_o are the initial particle locations at time $t = 0$ s, g is the gravity and τ is the particle relaxation time, which is defined as $\tau = \rho d_p^2/18\mu$. The inherent downfall of enabling a simple analytical solution for the particle motion equation is the uniform free-stream velocity assumption which does not account for changes in the velocity field, particularly in the vicinity of the human body and face. Instead, a numerical method based on the Runge–Kutta scheme is used to track

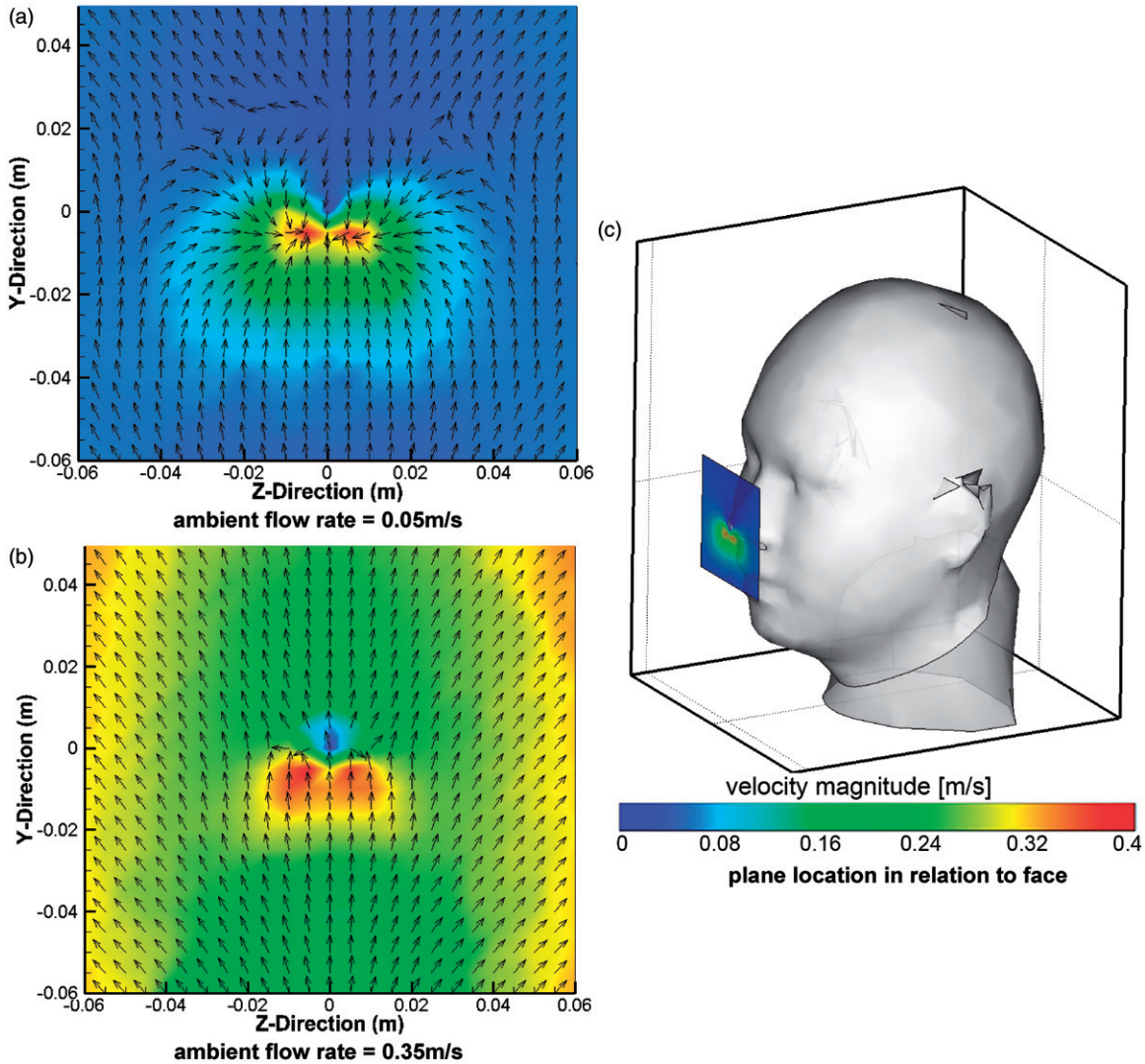

Figure 4. Frontal view of upstream velocity magnitude contour overlayed with 2D cross-stream (y–z components) vector flow field. The coordinate $y = 0$ m is the height of the nostril inlets, and $z = 0$ m is the midline of the mannequin. The plane location is 0.01 m upstream from the nose.

particles in a 2D plane. Figure 5 shows single representative trajectory for 1, 10, 40 and 80 μm particles. The particles are released from different upstream plane locations of 20, 50 and 100 cm from the nose tip to investigate the trajectories and to determine if the particle trajectory is consistent for different upstream source locations. The trajectories are overlaid onto the free-stream velocity vectors in the plane which gives an indication of the potential influence of the surrounding air on the particle transport. As before, the coordinates have the origin x, y (0, 0) located at the nostrils and therefore the trajectories of the inhaled particles will all converge to the origin.

First, inhaled smaller particles (1 and 10 μm) move within a narrow range in the vertical direction (y component) compared with that for larger particles (40 and 80 μm). The smaller particles are influenced considerably by the free-stream flow where the particles are transported from a location that is below the nostril openings and this is more evident for a faster free-stream velocity. For the larger particles, gravitational acceleration is overriding and the particle source location must exist at much higher distances above the nostril inlets. At the faster free-stream velocity of 0.35 m s^{-1}, the influence of the free stream has a greater influence on 40 μm particles than the gravitational force. This physical behavior is encapsulated through the particle relaxation time which defines the particle terminal velocity. For the particles used, 1, 10, 40 and 80 μm, the corresponding terminal velocities are 3.48×10^{-5} m s^{-1}, 3.06×10^{-3} m s^{-1}, 4.84×10^{-2} m s^{-1} and 1.72×10^{-1} m s^{-1}, respectively. It should be noted that 80 μm particles are outside the Stokes regime.

It should be noted that the particles were released from rest to mimic a source that is disturbed to release the particles. For particles released at zero velocity versus at the free-stream velocity and their terminal settling velocity, there would not be significant difference for 1 and 10 μm particles. However, the 40 and 80 μm particles have larger relaxation times and their trajectories will be influenced. From their initial velocity of zero, particles take a short period of time (approximately 0.06 s for the 80 μm particles) to reach equilibrium with the free-stream air and achieve their terminal settling velocity. During this 0.06 s period, 80 μm particles introduced at rest will travel about 70% of the horizontal distance of those introduced at the free-stream velocity.

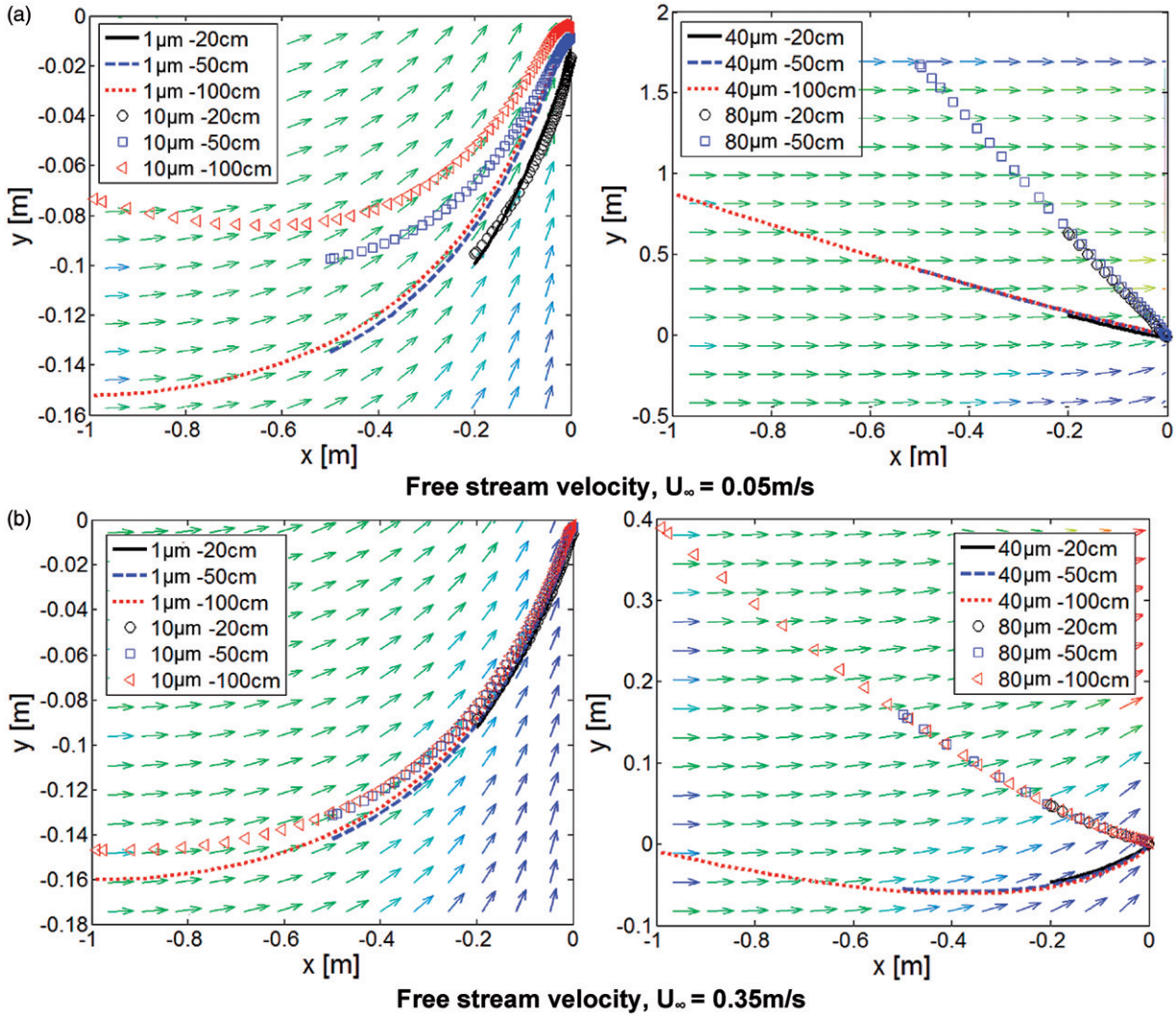

Figure 5. Particle trajectories represented by symbols (10 and 80 µm) and lines (1 and 40 µm) released from different upstream locations from the nostrils (*x*-axis) and at free-stream velocities of (a) $U_\infty = 0.05\,\mathrm{m\,s^{-1}}$ and $U_\infty = 0.35\,\mathrm{m\,s^{-1}}$. Velocity vectors in the background are colored by its magnitude with red being the peak velocity and blue the minimum velocity.

For the closest release plane (i.e. 0.2 m) in our simulations, introducing particles at rest may result in up to a 3% difference in their horizontal and vertical position relative to particles introduced at the free-stream velocity and their terminal settling velocity. This difference decreases to less than 1% for 40 µm particles. Thus, introduction of particles at rest versus at an equilibrium state should minimally affect our results.

The influence of different upstream locations from which the particles were released only differ for the smaller particles especially where the free-stream velocity is $0.05\,\mathrm{m\,s^{-1}}$. Near the face, free-stream velocity vectors are dominant in the vertical direction and therefore particles closer to the body must originate from a lower position, whereas the particles released further upstream are less influenced by the sharp gradients near the body. For the larger particles, its mass and size dominate and the representative path from 1.0 m upstream is consistent with the other shorter upstream distances from the nostrils. This result has important implications that should be considered during experimental exposure studies, particularly in wind tunnel studies where a particle source is released from a given location/distance from the human mannequin. Furthermore, the results reinforce the effectiveness of well-mixed environments as a means for inhalation testing, although this is often difficult to achieve experimentally.

Inhaled particles

The origins of all inhaled particles are traced back to their release location form an enclosed area A_c, which is referred to as the critical area (Vincent et al., 1990). Figure 6 shows the shape and vertical location of each critical area for 1, 40 and 80 µm particles in relation to the nostril height. The influence of gravitational settling on large particle diameters determines the height of the particle source that is likely to be inhaled, as discussed earlier. The influence of free-stream velocity on the critical areas for each particle size can be compared simultaneously as the results are presented on a common scale. As free-stream velocity increases, the critical areas become smaller and the difference in the vertical height origin for 1 and 80 µm particles is reduced. Furthermore, the source location for small particles (i.e., roughly <2.5 µm) that are likely to be inhaled are located very close to each other especially when the free-stream velocity increases.

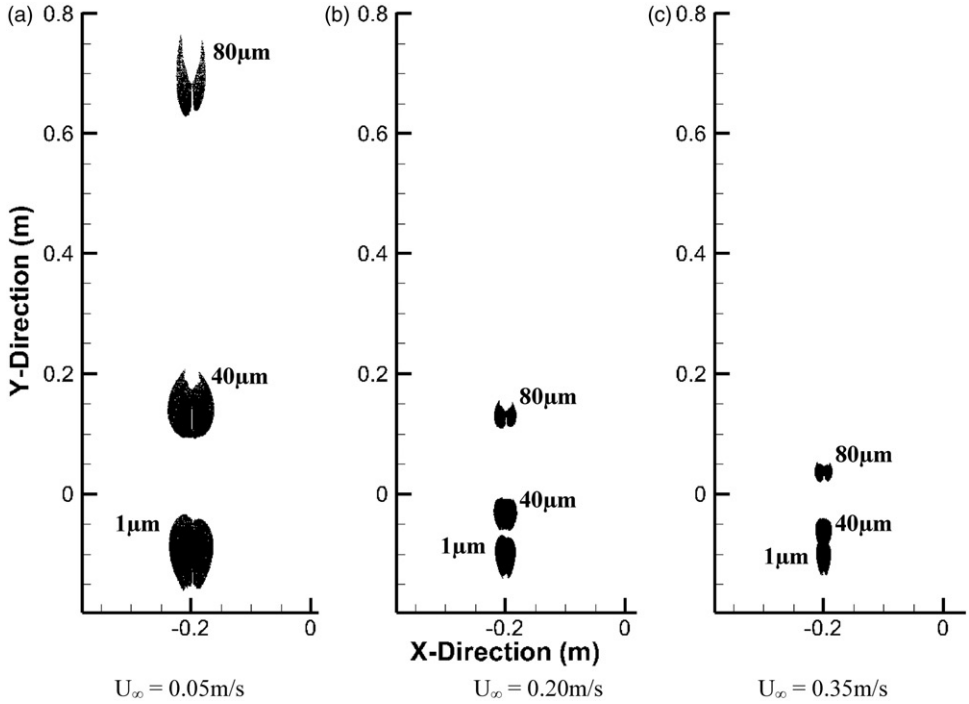

Figure 6. Critical areas for 1, 40 and 80 µm particle sizes released from a plane 20 cm upstream from the nostril inlets for different free-stream velocities, U_∞. The nostrils are located at the coordinates (0, 0).

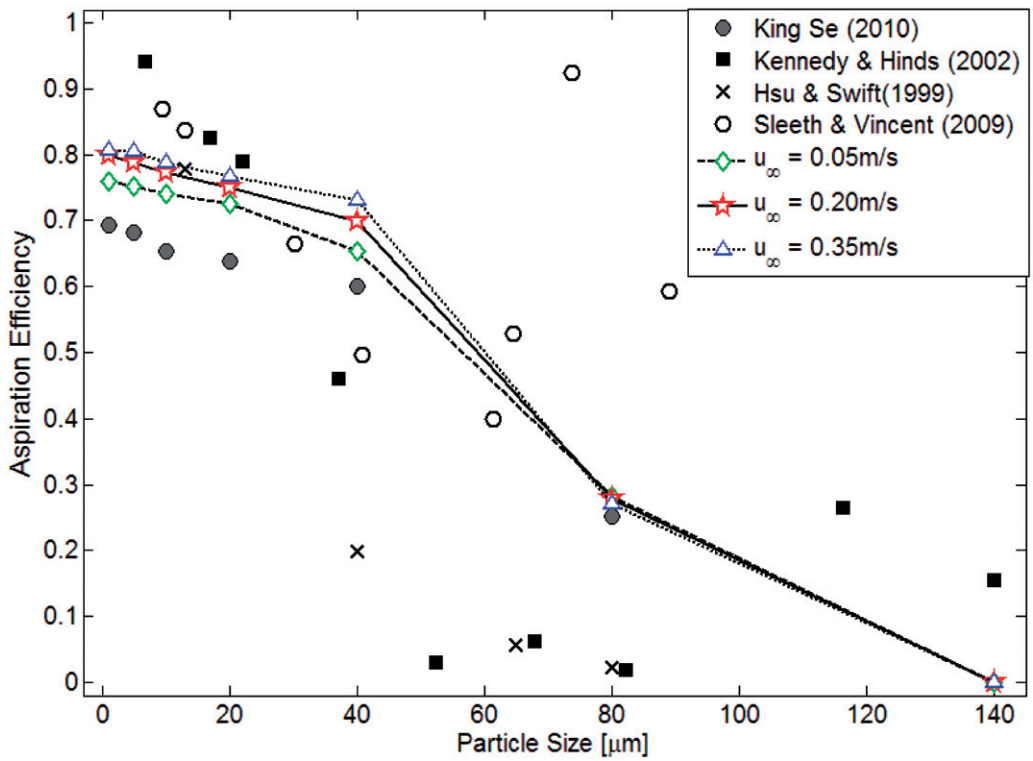

Figure 7. Nasal aspiration efficiencies facing into the wind for the different free-stream velocity. Comparisons are made with the numerical predictions of: King Se et al. (2010) inhalation rate = 15 L min^{-1}, U_∞ = 0.20 m s^{-1}; Kennedy & Hinds (2002) inhalation rate = 14.2–37.3 L min^{-1}, U_∞ = 0.4–1.6 m s^{-1}; Hsu & Swift (1999) inhalation rate = 12 L min^{-1}, U_∞ = 0 m s^{-1} and; Sleeth & Vincent (2009) inhalation rate = 6.0 and 20.0 L min^{-1}, U_∞ = 0.1–0.42 m s^{-1}.

This means that during inhalation exposure studies, it can be assumed that smaller particle sizes (within the respirable range) that are captured should originate from nearly the same locations. Thus, predictions of where and how particles are transported through the surrounding flow field can be surmised. For particles released at the free-stream velocity, the additional horizontal stopping distance means that the new critical area location for 40 and 80 µm particles are slightly lower while for 1 and 10 µm there would be negligible difference.

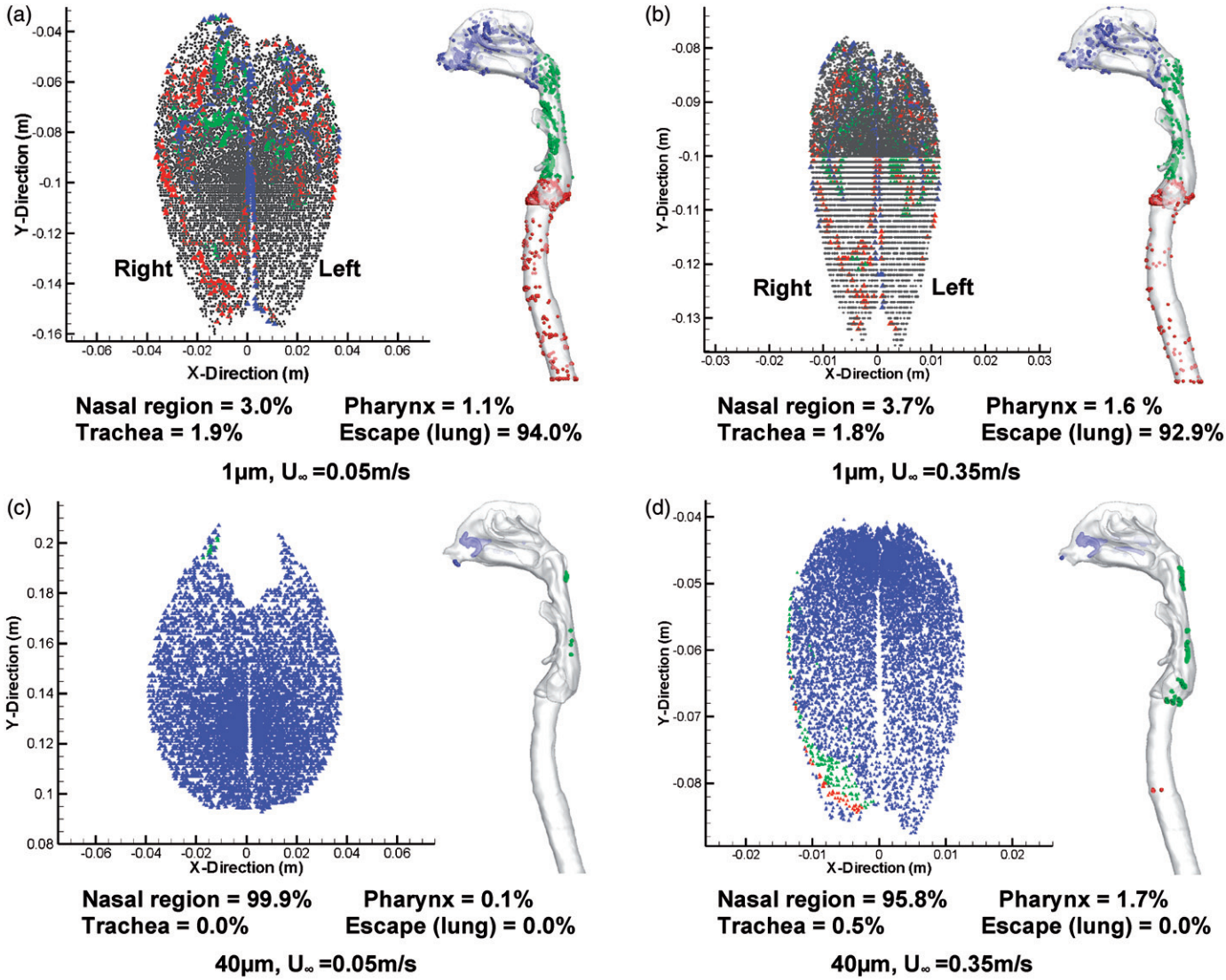

Figure 8. Critical areas for inhaled 1 and 40 μm, and its deposition in the upper respiratory airway for free-stream velocities of 0.05 and 0.35 m s^{-1}. Inhalation rate is 15 L min^{-1}.

The AE curve for nose breathing with the facing-the-wind orientation is given in Figure 7. The results are produced from a source located 20 cm upstream from the nose. The results show a decreasing AE with an increase in the particle size. The AE decreases gradually from approximately 80% to 70% for particles in the size range of 1–40 μm that were evaluated. There is then a sharp drop for 80 μm particles which had an AE of approximately 30%. Comparison with experimental data (Hsu & Swift, 1999; Kennedy & Hinds, 2002; Sleeth & Vincent, 2009) and numerical predictions (King Se et al., 2010) show some consistency among the work. It should be noted that the data point for 116 μm particles in the study by Kennedy & Hinds (2002) reported a large uncertainty of approximately ±30%. The data for Hsu & Swift (1999) is based on a torso mannequin placed in calm air at rest nasal breathing condition (12 L min^{-1}), while for Sleeth & Vincent (2009), ultra-low wind speed environments of 0.1–0.5 m s^{-1} was used. The free-stream velocities undertaken in this study were low velocities between 0.05 and 0.35 m s^{-1}. The influence on the flow patterns in the breathing region was shown earlier in Figure 4. For particle inhalation, an increase in the free-stream velocity caused an increase in the inhalability of particles in the size range of 1–40 μm. For 80 μm particles that exhibit greater inertial property, there was significant change in AE. In earlier studies, generally it has been found that particle inhalability increases with wind speeds in the range of 1–8 m s^{-1} (Vincent et al., 1990), and in particular for particles of range 50–100 μm that was evaluated. Further analysis was performed for particles released from 100 cm upstream, which found a small increase for 1 μm (6% in the AE), while for 40 μm particles, a negligible change, e.g. <1% was found.

The inhalation was simulated as a steady constant flow rate in place of a realistic cyclic unsteady flow to emphasize the influence of particle trajectories from different source locations. The assumption of an averaged steady or quasi-steady flow in place of a cyclic inhalation can be sufficient where the Womersley frequency number is less than 1 (Inthavong et al., 2008). The influence of unsteady inhalation on the AE may be deduced by considering the particle inertia during the cyclic inhalation pattern. During the accelerated and peak regions of inhalation, higher velocities will induce an increased AE in

small particles; however, this may then be countered by the deceleration and minimum velocity regions of inhalation. For larger particles (>>10 μm), the influence of unsteady inhalation will be less pronounced.

In determining the dosimetry due to exposure to a contaminant source, the deposition of inhaled particles inside the respiratory airway can serve as a predictive tool to guide dosimetry calculations. Each individual particle found in the critical area is registered and its deposition in the respiratory airway or its escape through the trachea matched. Figure 8 shows each particle colored by regional deposition in the respiratory airway where blue represents deposition in the nasal cavity region; green represents the pharyngeal region; red represents the tracheal region and grey represents those particles that pass through the trachea and into the bronchial region of the lungs. For 1 μm particles, there is no distinguishable pattern from the critical area that can allow confident predictions of where a particle may deposit within the respiratory airway. The percentage of 1 μm particles reaching the lung region is very high with approximately 93% of all inhaled particles passing through. Furthermore, the deposition efficiencies do not vary for the different free-stream flow rates. For 40 μm particles, the critical area shape changes significantly when the free-stream velocity increases from 0.05 to 0.35 m s^{-1} which are consistent with the results shown earlier. In addition, the deposition patterns in the respiratory airway also change where more particles deposit later in the pharynx at the higher flow rate. There is a high concentration of particles found just past the nostril inlets, which is a preferential region of deposition. This result can allow insight and better risk assessments of inhalation exposure to contaminant sources. For example, long-term exposure to particles around the 40 μm size range (e.g. wood dust) may contribute toward the causative reasoning for reported nasal dysfunction.

Conclusion

An integrated computational model that includes the respiratory airway inside a human mannequin and placed in a room was created for simulations to determine the trajectories of airborne particle caused by the free-stream flow field and inhalation from the mannequin. The flow field in the free stream was mainly uniform until it reached the near body region, e.g. <5 cm from body. Velocity vectors provided visualization revealing that in the near breathing region vectors point vertically upward, because of the presence of the torso. This vertical direction becomes increasingly important for the smaller, 1 and 10 μm, particles as they are transported from the contaminant source to the nostril inlets. Inhaled particles formed an enclosed area from where they originate, creating a region known as the critical area. It was shown that as the free-stream velocity increases, the critical areas become smaller and the difference in the vertical height origin for 1 and 80 μm is reduced. For each critical area, the technique of registering each individual particle and determining its local deposition site was applied. This allows a correlation to be inferred for the contaminant source and its likelihood of deposition in different regions of the respiratory airway. This study aimed to establish a better understanding of inhalation exposure and to enhance the current state-of-the-art CFD modeling leading to a more holistic approach in future computational exposure studies.

Declaration of interests

The authors declare that there are no conflict of interests in the production of this work. The authors gratefully acknowledge the financial support provided by the National Basic Research Program (973) of China, Grant No. 2012CB720100, and the Australian Research Council (project ID: DP120103958).

References

Agranovski IE, Pyankov OV, Altman IS. (2005). Bioaerosol contamination of ambient air as the result of opening envelopes containing microbial materials. Aerosol Sci Technol 39:1048–55.

Anthony TR, Flynn MR, Eisner A. (2005). Evaluation of facial features on particle inhalation. Annals Occup Hyg 49:179–93.

Baldwin PEJ, Maynard AD. (1998). A survey of wind speeds in indoor workplaces. Ann Occup Hyg 42:303–13.

Bolashikov ZD, Melikov AK, Kierat W, et al. (2012). Exposure of health care workers and occupants to coughed airborne pathogens in a double-bed hospital patient room with overhead mixing ventilation. HVAC&R Res 18:602–15.

Doorly DJ, Taylor DJ, Gambaruto AM, et al. (2008). Nasal architecture: form and flow. Philos Trans Royal Soc A: Math Phy Eng Sci 366: 3225–46.

Ganor E, Fischbein A, Brenner S, Froom P. (1992). Extreme airborne asbestos concentrations in a public building. British J Indust Med 49: 486–8.

Ge Q, Li X, Inthavong K, et al. (2013). Numerical study of the effects of human body heat on particle transport and inhalation in indoor environment. Buil Environ 59:1–9.

Golshahi L, Finlay WH, Olfert JS, Tu J. (2010). Deposition of inhaled ultrafine aerosols in replicas of nasal airways of infants. Aerosol Sci Technol 44:741–52.

Hofmann W, Golser R, Balashazy I. (2003). Inspiratory deposition efficiency of ultrafine particles in a human airway bifurcation model. Aerosol Sci Technol 37:988–94.

Hsu DJ, Swift DL. (1999). The measurement of human inhalability of ultralarge aerosols in calm air using manikins. J Aerosol Sci 30: 1331–43.

Huston RL. (2009). Principles of biomechanics. UK: CRC Press, Taylor and Francis Group.

Inthavong K, Ge Q, Se CMK, et al. (2011a). Simulation of sprayed particle deposition in a human nasal cavity including a nasal spray device. J Aerosol Sci 42:100–13.

Inthavong K, Tu JY, Ahmadi G. (2009). Computational modelling of gas-particle flows with different particle morphology in the human nasal cavity. J Comput Multiphase Flows 1:57–82.

Inthavong K, Tu J, Heschl C. (2011b). Micron particle deposition in the nasal cavity using the v2–f model. Comput Fluids 51:184–8.

Inthavong K, Wen J, Tian ZF, Tu JY. (2008). Numerical study of fibre deposition in a human nasal cavity. J Aerosol Sci 39:253–65.

Inthavong K, Zhang K, Tu J. (2011c). Numerical modelling of nanoparticle deposition in the nasal cavity and the tracheobronchial airway. Comput Meth Biomech Biomed Eng 14:633–43.

Isabey D, Chang HK. (1981). Steady and unsteady pressure-flow relationships in central airways. J Appl Physiol 51:1338–48.

Kelland P. (1992). Sick building syndrome, working environments and hospital staff. Indoor Built Environment 1:335–40.

Kennedy NJ, Hinds WC. (2002). Inhalability of large solid particles. J Aerosol Sci 33:237–55.

King Se CM, Inthavong K, Tu J. (2010). Inhalability of micron particles through the nose and mouth. Inhalation Toxicology 22:287–300.

Lee J-H, Na Y, Kim S-K, Chung SK. (2010). Unsteady flow characteristics through a human nasal airway. Res Physiol Neurobiol 172: 136–46.

Li J, Yavuz I, Celik I, Guffey S. (2007). Predicting worker exposure—The effect of ventilation velocity, free-stream turbulence and thermal condition. J Occup Environ Hyg 4:864–74.

Longest PW, Tian G, Walenga RL, Hindle M. (2012). Comparing MDI and DPI aerosol deposition using in vitro experiments and a new stochastic individual path (SIP) model of the conducting airways. Pharmaceutical Res 29:1670–88.

Matida EA, Finlay WH, Lange CF, Grgic B. (2004). Improved numerical simulation for aerosol deposition in an idealized mouth-throat. J Aerosol Sci 35:1–19.

Menter FR, Langtry RB, Likki SR, et al. (2006). A correlation-based transition model using local variables—part I: model formulation. J Turbomachinery 128:413–22.

Moghadas H, Abouali O, Faramarzi A, Ahmadi G. (2011). Numerical investigation of septal deviation effect on deposition of nano/microparticles in human nasal passage. Res Physiol Neurobiol 177: 9–18.

Morsi SA, Alexander AJ. (1972). An investigation of particle trajectories in two-phase flow systems. J Fluid Mech 55:193–208.

Namieśnik J, Górecki T, Kozdroń-Zabiega ła B, Lukasiak J. (1992). Indoor air quality (IAQ), pollutants, their sources and concentration levels. Buil Envir 27:339–56.

Nazaroff W. (2004). Indoor particle dynamics. Indoor Air 14:175–83.

Repace JL. (1982). Indoor air pollution. Envir Internat 8:21–36.

Scott Duncan EJ, Kournikakis B, Ho J, Hill I. (2009). Pulmonary deposition of aerosolized bacillus atrophaeus in a swine model due to exposure from a simulated anthrax letter incident. Inhalation Toxicology 21:141–52.

Sleeth DK, Vincent JH. (2009). Inhalability for aerosols at ultra-low windspeeds. J Phy: Conf Ser 151:1670–88.

Vincent JH, Mark D, Miller BG, et al. (1990). Aerosol inhalability at higher windspeeds. J Aerosol Sc 21:577–86.

Zhang Z, Kleinstreuer C. (2011). Laminar-to-turbulent fluid–nanoparticle dynamics simulations: model comparisons and nanoparticle-deposition applications. Internat J Num Meth Biomed Eng 27: 1930–50.

Zhu JH, Lee, HP, Lim KM, et al. (2011). Evaluation and comparison of nasal airway flow patterns among three subjects from Caucasian, Chinese and Indian ethnic groups using computational fluid dynamics simulation. Resp Physiol Neurobiol 175:62–9.

Zhuang Z, Landsittel D, Benson S, et al. (2010). Facial anthropometric differences among gender, ethnicity, and age groups. Annal Occup Hyg 54:391–402.